The 18th International Topical Meeting on Nuclear Reactor Thermalhydraulics, NURETH-19
Portland, OR, USA, August 18-23, 2019

Log Number: 27469

NUMERICAL SIMULATIONS OF TURBULENT RAYLEIGH-BÉNARD CONVECTION WITH A FREE SURFACE

W. A. Hay[1], V. Deledicque[2] and M. V. Papalexandris[1]

[1]Université catholique de Louvain ,
Institute of Mechanics, Materials and Civil Engineering,
B-1348 Louvain-la-Neuve, Belgium
[2]Bel V, Rue Walcourt 148, 1070 Anderlecht, Belgium

william.hay@uclouvain.be

ABSTRACT

One fundamental conclusion from the OECD 2018 PIRT study on Loss of Cooling Accidents (LOCAs) in Spent Fuel Pools (SFPs) was the urgent need for improved understanding of single and two-phase natural convection phenomena during the pre-uncovery phase. Even before nucleation, complex thermal mixing and evaporation phenomena coexist. Further, the equilibrium temperature reached by a pool and the volume of gas above during a SFP-LOCA can exceed 80°C. The variation in fluid properties during heat-up means that the Oberbeck-Boussinesq approximation cannot be utilized in numerical simulations for the problem in hand and that a low-Mach number approximation of the governing equations must be implemented.

The aforementioned physical phenomena can still be captured when the upper pool volume is modeled as a cavity heated from below with a free surface, allowing for simultaneous study of turbulent natural convection and free-surface evaporation. The motivation of our research is therefore to carry out non-Oberbeck-Boussinesq numerical simulations of turbulent Rayleigh-Bénard convection to better understand the impact of the free surface boundary condition.

Our low-Mach number solver is first validated against experimental data for a wall-bounded Rayleigh-Bénard Convection (RBC) flow up to Rayleigh numbers of 10^8. Subsequently, we simulate the case of water heated from below with a free surface with air, the gaseous domain being closed with a free-slip boundary. Our studies dynamically calculate the interfacial temperature and Rayleigh numbers during heat-up and assess the impact on the Large-Scale Circulation (LSC) and on the Nusselt number. Further, they contribute towards the ultimate goal of assessing the role of turbulence on free-surface evaporation during an SFP-LOCA.

Introduction

Following the events of Fukushima in 2011 numerous international efforts have been made to improve knowledge and better understanding of Loss-of-Cooling/Coolant-Accidents (LOCA) in Spent Fuel Pools (SFP). A Phenomena Identification and Ranking Table (PIRT) exercise has been commissioned on the subject by the OECD. One of the issues highlighted was the capability of currently available computational codes to accurately capture the single and multiphase physical phenomena occurring in the early-stages of the accident. The research presented herein is in collaboration with the DENOPI project which serves as a basis for model development and validation of numerical simulation tools for the SFP-LOCA.

Our research focuses on the early stages of the accident, specifically the period from the beginning of Station Blackout (SBO) until the fuel racks are first uncovered. Within this period the physical phenomena that we are concerned with are turbulent natural convection and free surface evaporation. Nucleation, both homogeneous and inhomogeneous, are not considered. The intention herein is to gain a better understanding of the inter-dependent nature of the liquid-side turbulent structures and the evaporation rates at the free surface. In order to capture accurately these phenomena, it is necessary to make a significant geometric simplification of the problem. We do this by considering only the upper pool volume, the fuel assemblies are represented as a flat heated bottom wall, the upper volume of the SFP is represented by a cubic domain and the atmosphere above by an air phase of finite volume. This simplification allows us to ignore the complicated geometry of the fuel racks, whilst still capturing the relevant physics. It is noted however that this significant geometric simplification removes from the problem the upward flow currents emanating from would-be fuel assemblies below and the respective downward currents at the walls of the SFP.

Further, in this paper we ignore free-surface evaporation and assess the impact of the free surface on the flow and thermal dynamic structures below. With the above simplifications we end-up with a pseudo-Rayleigh-Bénard Convection (RBC) set-up with a free surface upper boundary. Classical RBC is a fundamental problem in fluid dynamics where an Oberbeck-Boussinesq fluid layer is uniformly heated from below and uniformly cooled from above. Turbulent RBC typically occurs when the layer is extended in height so as to increase the Rayleigh number above a critical value; it is an extensively researched subject both experimentally and numerically (see [**Siggia**] and [**Ahlers**] for reviews on the topic). The richness of results allowed Grossman & Lohse [**Grossman2000**] -[**Grossman2004**] to develop a theory to account for Nusselt and Reynolds number dependencies on Rayleigh and Prandtl number parameter ranges. The extension to Non-Oberbeck-Boussinesq flows is covered in [**Ahlers2007**] and [**Sugiyama**]. Although it is noted that the initial experiments of classical RBC by Bénard had a free surface, the impact of the free surface on *turbulent* RBC is not yet known. The historical reason for this was the requirement for extremely well-controlled conditions, which a rigid upper boundary was able to provide.

The outline of the paper is as follows. In Section 2 we provide an overview of the physical phenomena and the governing equations, in Section 3 the numerical method is given with a description of the low-Mach number numerical algorithm, in Section 4 a validation exercise for a classical RBC problem is carried out, in Section 5 we present results for a two-phase case at moderate, yet turbulent, Rayleigh number and in Section 6 we make conclusions.

Governing Equations

RBC can be summarized as a container heated from below and cooled from above. The system is determined by the three dimensionless control parameters of Rayleigh number (Ra), Prandtl number (Pr) and aspect ratio (Γ).

$$\mathrm{Ra} = \frac{|\mathbf{g}|\beta\Delta\mathrm{T}\mathrm{L}^3}{\nu\kappa},$$
$$\mathrm{Pr} = \frac{\nu}{\kappa},$$
$$\Gamma = \frac{\mathrm{H}}{\mathrm{W}} = 1.$$

Where $|\mathbf{g}|$ is the magnitude of gravitational acceleration, β is the thermal expansion coefficient, H and W are the height and width of the domain respectively, ν is the kinematic viscosity, ΔT is the temperature difference between the top and bottom boundaries and κ is the thermal diffusivity. The system response to a given Ra, Pr and Γ is measured in a dimensionless heat flux (Nusselt number, Nu) and a turbulence (Reynolds number, Re); for which the velocity is representative of the Large Scale Circulation (LSC), or mean wind [**Ahlers**]. Numerical simulations can provide insight into the role played by the upper boundary condition on these system responses.

The working fluids are a liquid (water) and a gas (air), treated as immiscible Newtonian fluids for which we solve a single momentum equation by assuming a volume-averaged mixture velocity. In the flow studied, significant changes in density occur gas-side, implying that inertial effects must be captured. For this reason, the system of governing equations is the low-Mach number approximation of the compressible Navier-Stokes equations [**Majda**], which reads in dimensional form,

$$\frac{\partial\rho}{\partial t} + \nabla\cdot(\rho\mathbf{u}) = 0, \tag{1}$$

$$\frac{\partial(\rho\mathbf{u})}{\partial t} + \nabla\cdot(\rho\mathbf{u}\mathbf{u}) = \nabla\cdot\tau - \nabla\mathrm{p}_1 + \rho\mathbf{g}, \tag{2}$$

$$\frac{\partial\left(\rho\mathrm{C}_\mathrm{p}\mathrm{T}\right)}{\partial t} + \nabla\cdot\left(\rho\mathbf{u}\mathrm{C}_\mathrm{p}\mathrm{T}\right) = \nabla\cdot(\lambda\nabla\mathrm{T}) + \frac{\mathrm{dp}_0(\mathrm{t})}{\mathrm{d}t}. \tag{3}$$

In Equation (2), p_1 is the 2nd-order component of the low-Mach number expansion of the pressure, it is interpreted as the dynamic pressure familiar to those working in incompressible flows. τ is the deviatoric part of the viscous stress tensor given below where $\mathbf{I}$ is the identity matrix and μ the dynamic viscosity,

$$\tau = \mu\left(\nabla\mathbf{u} + (\nabla\mathbf{u})^\mathrm{T} - \frac{2}{3}(\nabla\cdot\mathbf{u})\mathbf{I}\right). \tag{4}$$

In Equation (3), C_p is the specific heat, λ the thermal conductivity and p_0 the 1st-order component of the low-Mach number expansion of the pressure. The quantity p_0 is referred to as the thermodynamic pressure. According to the low-Mach-number expansion, it is spatially uniform and a function of time only. For open domains, p_0 is equal to the ambient pressure, whereas for closed domains it varies with time. In the latter case, since the mass of the fluid remains constant, p_0 can be calculated by integrating the equation of state over the flow domain [**Lessani2006**]. In particular, for an ideal gas, p_0 is calculated as follows,

$$p_0 = \frac{M_G R_G}{\int_{V_G} (1/T) dV}. \tag{5}$$

In this relation, M_G is the total mass of gas inside the closed domain occupying the volume V_G and R_G is the universal gas constant. Herein, the air is treated as an ideal gas, i.e.

$$\rho_G = \frac{p_0}{R_G T}, \tag{6}$$

We thus calculate p_0 by integrating the above equation over the volume occupied by the gas and we assign the same value at the liquid side too. In order to close the system of governing equations, we implement a polynomial relation for the water density, where coefficients originate from a fit to tabulated data of [**Wagner**] over the range of interest.

$$\rho_L = c_3 T^3 + c_2 T^2 + c_1 T + c_0. \tag{7}$$

All further liquid properties, λ, C_p and μ, are also obtained via temperature polynomial functions of the same order. The same is true for C_p and C_v of the gas. We obtain the dynamic viscosity from a Sutherland law [**Sutherland**]

$$\mu = \frac{A_s \sqrt{T}}{1 + T_s/T}. \tag{8}$$

In this relation, parameters A_s and T_s take values of 1.672e-06 and 170.672K respectively. Finally, the thermal conductivity is found from a modified Euken model [**Poling**].

$$\frac{\lambda}{\mu C_v} = 1.32 + \frac{1.77 R_G}{C_v}. \tag{9}$$

Numerical method

In this section we first outline the interfacial treatment before summarizing the velocity-pressure coupling method and the overall solution algorithm.

Interface treatment

To capture the interface between two immiscible fluids we implement the Volume-of-Fluid (VOF) method [**Hirt**]. In the VOF method an indicator function, f, is introduced which allows the interface location to be defined in the domain. For numerical purposes, f represents the fraction of a computational grid cell occupied by liquid and can be understood as the liquid volume fraction field. In the case studied here, the remaining fraction is filled with a single gas phase (air). Consequently, the following statement is made

$$f = \begin{cases} 0 & \text{gas,} \\ 0 < f < 1 & \text{at an interface,} \\ 1 & \text{liquid.} \end{cases}$$

The volume-averaged fluid properties: ρ, μ, ρC_P and λ, are then calculated based on the volume fraction field in the grid cell via the following

$$\varphi = f\varphi + (1-f)\varphi\,.$$

The interface is then advected via the following

$$\frac{\partial f}{\partial t} + \nabla \cdot (\mathbf{u} f) = 0\,. \tag{10}$$

A successful VOF method will both minimize diffusion of the interface across grid cells and keep the volume fraction bounded between 0 and 1. The specific VOF algorithm used here is the incompressible VOF solver included in the open-source CFD package OpenFOAM [**Rusche**]. It is different to the majority of VOF packages in that the interface is not reconstructed geometrically, which is the standard way to ensure a sharp interface. The crisp capture of the interface in OpenFOAM is assured by introducing an artificial interfacial compression term to (10) as follows

$$\frac{\partial f}{\partial t} + \nabla \cdot (\mathbf{u} f) + \nabla \cdot (|\mathbf{u}| \cdot \boldsymbol{n}\,[f\,(f-1)]) = 0\,. \tag{11}$$

Where $\boldsymbol{n}$ is the normal vector at the interface, directed from liquid to gas, and the $f(f-1)$ term ensures that the compression uniquely occurs in interfacial grid cells. The volume fraction is kept bounded by solving (11) using an explicit solution algorithm and flux-limiting.

Pressure-velocity coupling

Before summarizing the overall algorithm, it is first necessary to introduce the pressure-velocity coupling algorithm used. A PISO-type projection method is used, similar to [**Issa**] and [**Oliviera**], which results in a variable coefficient Poisson equation being solved for p_1. We work on the assumption that the liquid is incompressible and the gas is under low-Mach number conditions. This means that the linear elliptic equation for p_1 has different source terms depending on the volume fraction of the grid cell in question, this is now summarized for clarity.

Equations (1) and (2) can be rewritten in the following form

$$\nabla \cdot \mathbf{u} = -\frac{1}{\rho}\frac{D\rho}{Dt}, \tag{12}$$

$$\frac{D\mathrm{T}}{Dt} = \frac{1}{\rho \mathrm{C_P}}\frac{\mathrm{dp_0(t)}}{\mathrm{d}t} + \frac{1}{\rho \mathrm{C_P}}\nabla \cdot (\lambda \nabla \mathrm{T}) \,. \tag{13}$$

Use of the chain rule transforms Equation (12) into

$$\nabla \cdot \mathbf{u} = \begin{cases} -\frac{1}{\rho}\left(\frac{\partial \rho}{\partial \mathrm{T}}\right)_{\mathrm{p_0}} \frac{D\mathrm{T}}{Dt} - \frac{1}{\rho}\left(\frac{\partial \rho}{\partial \mathrm{p_0}}\right)_{\mathrm{T}} \frac{\mathrm{dp_0(t)}}{\mathrm{d}t} & \text{gas}\,, \\ -\frac{1}{\rho}\left(\frac{\mathrm{d}\rho}{\mathrm{dT}}\right)_{\mathrm{p_0}} \frac{D\mathrm{T}}{Dt} & \text{liquid}\,. \end{cases} \tag{14}$$

where we obtain the two $\left(\frac{\partial \rho}{\partial \mathrm{T}}\right)_{\mathrm{p_0}}$ terms by differentiating the equations of state with respect to T. Similarly, for the gas we obtain $\left(\frac{\partial \rho}{\partial \mathrm{p_0}}\right)_{\mathrm{T}}$ by differentiating the ideal gas law with respect to $\mathrm{p_0}$. Substituting Equation (13) into (14) and manipulating gives the final velocity divergence terms to be used in the modified PISO algorithm.

$$\nabla \cdot \mathbf{u} = \begin{cases} -\frac{1}{\gamma \mathrm{p_0}}\frac{\mathrm{dp_0(t)}}{\mathrm{d}t} + \frac{\gamma - 1}{\gamma \mathrm{p_0}}\nabla \cdot (\lambda \nabla \mathrm{T}) & \text{gas}\,, \\ -\frac{1}{\rho^2 \mathrm{C_p}}\frac{\mathrm{d}\rho}{\mathrm{dT}}\left(\frac{\mathrm{dp_0(t)}}{\mathrm{d}t} + \nabla \cdot (\lambda \nabla \mathrm{T})\right) & \text{liquid}\,. \end{cases} \tag{15}$$

In practice, the liquid velocity divergence term is very close to zero as a result of both $\frac{1}{\rho^2 \mathrm{C_p}}$ and $\frac{\mathrm{d}\rho}{\mathrm{dT}}$ being very small.

The robustness of the flow solver is improved by encorporating the buoyancy term inside the hydrodynamic pressure gradient term in the momentum equation [**Georgiou**]. The semi-discretized momentum equation for a control volume is then written as

$$A_p U_p + \sum_N A_N U_N - \frac{U^0}{\Delta t} = -\nabla \mathrm{p}_1 - \mathbf{g}\cdot\mathbf{h}\nabla\rho\,. \tag{16}$$

Where A_P represents the diagonal coefficient and A_N off-diagonal coefficients for a control volume P, $\sum_N$ denotes the sum over neighboring faces. Rearranging gives a relation for the velocity at point P

$$U_p = \frac{1}{A_p}H(U) - \frac{1}{A_p}\nabla \mathrm{p}_1 - \frac{1}{A_p}\mathbf{g}\cdot\mathbf{h}\nabla\rho\,. \tag{17}$$

Where $H(U) = -\sum_N A_N U_N + \frac{U^0}{\Delta t}$. Taking the divergence of the above relation and introducing equation (15) for the velocity divergence, results in the following linear elliptic equation

$$\nabla\cdot\left(\frac{1}{A_p}\nabla \mathrm{p}_1\right) = \nabla\cdot\left(\frac{1}{A_p}H(U) - \frac{1}{A_p}\mathbf{g}\cdot\mathbf{h}\nabla\rho\right) + \frac{1}{\gamma \mathrm{p}_0}\frac{\mathrm{dp}_0}{\mathrm{d}t} + \frac{\gamma-1}{\gamma \mathrm{p}_0}\nabla\cdot(\lambda\nabla \mathrm{T})\,. \tag{18}$$

For the interfacial and liquid cells, the above equation is identical but the last term on the right-hand size is zeroed. In future work, when evaporation will be introduced, the interfacial divergence term will be determined by the evaporation rate.

Overall solution algorithm

Equations (1), (2), (3) and (11) represent the system of equations that must be solved. The overall algorithm is summarized as follows:

1. Solve equation (11) for $f^{\mathrm{n}+1}$,
2. Update ρ^* and corresponding mass fluxes,
3. Solve equation (3) for $T^{\mathrm{n}+1}$,
4. Update $\rho^{\mathrm{n}+1}$ and $\mathrm{p}_0^{\mathrm{n}+1}$,
5. Formulate dynamic pressure "Poisson" equation from (1), (2) and (3) and solve for $\mathrm{p}_1^{\mathrm{n}+1}$,
6. Update $\mathbf{u}^{\mathrm{n}+1}$.

The governing equations are discretized on a collocated grid system using the flux interpolation technique implemented in OpenFOAM to avoid pressure odd-even decoupling [**Jasak**]. All convective terms, except that of the volume fraction equation, are discretized using second-order linear schemes, whereas for f, a second order upwind scheme with the Van Leer slope limiter is used. All diffusion terms are also discretized in a second-order manner. For reasons of stability the time integration is performed via a first-order Euler implicit method.

Validation tests

In this section we validate a simplified version of the algorithm outlined in Section 3. A single-phase adaptation is validated, meaning steps 1 and 2 in the overall solution algorithm are switched off; consequently, there is no interface present. Further, the validation is carried out against Direct Numerical Simulations under Oberbeck-Boussinesq conditions and hence small ΔT. Still, an agreement between the well-resolved DNS from the literature and our simulations serves to increase the confidence in the results produced in Section 5.

A classical RBC domain with water as the working fluid is modeled in a set-up shown in Figure 1. We apply no-slip boundary conditions on all walls. The lateral side-walls are perfectly adiabatic, top and bottom walls are isothermal at T_{cold} and T_{hot} respectively, T_{mean} is set to give a $Pr = 4.4$. We then vary Ra between 10^6 and 10^8 by increasing the domain dimensions.

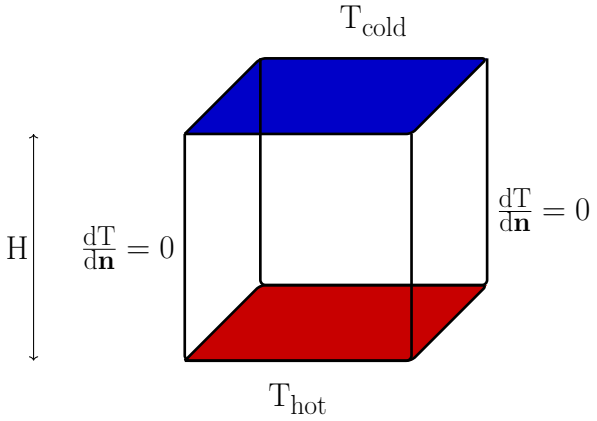

Figure 1 **Computational domain for the validation** : A classical RBC set-up of a cubic domain with water as the working fluid with adiabatic sidewalls and isothermal top and bottom. Velocity boundary conditions are no-slip at all walls

The use of DNS in RBC requires a refined grid to capture the Kolmogorov and Bachelor scales [**Grotzbach**]. This is achieved via a grid clustered near the walls and expanding towards the bulk via a hyperbolic tangent function. The refinement criteria for the bulk and boundary layers are found in [**StevensBulk**] and [**ShishkinaBL**] respectively.

A characteristic time-scale for the flow is the free-fall time, defined as $t_{ref} = H/u_{ref}$ where the free-fall velocity $u_{ref} = \sqrt{g\beta\Delta TH}$ [**Foroozani**]. We run simulations until they are statistically steady, here taken as 500 free-fall time units, and then take statistics over 500 more.

The Nusselt number in the domain is then calculated via the following relation (adapted from [**Shishkina**] to allow for variable density)

$$Nu_y = \sqrt{RaPr}\,\langle\hat{\rho}\hat{v}\hat{T}\rangle_{xzt} - \frac{\partial\langle\hat{T}\rangle_{xzt}}{\partial\hat{y}}\,. \tag{19}$$

In this equation, $\langle\cdot\rangle_{xzt}$ represents time and area averaging over any plane over the vertical direction. The vertical velocity component and temperature are non-dimensionalized as follows $\hat{v} = \frac{v}{u_{ref}}$ and $\hat{T} = \frac{T - T_{mean}}{\Delta T}$.

It is noted that Nu_y has two variable contributions: one convective and one diffusive, but Nu_y itself is constant along the vertical direction. The converged Nu_y values are given in Table 1 alongside the DNS results from the literature, showing that we obtain very good agreement with [**Kacz**].

Ra	Mesh	NP_θ	NP_u	Nu_y	Nu [**Kacz**]
10^6	64^3	6 (2.0)	8 (3.3)	8.3	8.4
10^7	110^3	8 (2.7)	13 (4.5)	16.3	16.1
10^8	168^3	6 (3.8)	9 (6.3)	32.3	32.2

Table 1 **Nusselt validation** : Simulation parameters and time and area averaged Nu_y. In each case the mesh is made up of an equal number of grid cells in all directions. NP_θ and NP_u represent the chosen number of grid points in the thermal and hydrodynamic boundary layers respectively (minimum values provided in parentheses)

Results for Turbulent RBC with a free surface

Numerical set-up

A schematic of the two-phase case set-up is provided in Figure 2. The temperature at the bottom wall is set uniformly to $T_{hot} = 325K$. This is below the representative cladding temperature for the early-stage of an SFP, however the omission of free surface evaporation is less consequential at lower pool temperatures. The side-walls are adiabatically insulated and the upper wall temperature is set to $T_{cold} = 280K$. This is below a representative air-side temperature of the SFP transient, however in order to obtain a ΔT across the pool ($T_{hot} - T_{int}$) whilst ignoring evaporation, a significant temperature drop is required across the computational domain. No-slip boundary conditions are applied at all walls except the upper wall, which is set to free slip. The domain is initially under atmospheric pressure conditions ($p_0 = 10^5$ Pa), but as explained in Section 2, p_0 varies in time.

The liquid-side of the computational domain is a cube; this domain is then extended vertically by a half to accommodate a gaseous phase, initially at rest. We first run a simulation at Ra = 10^5 until a statistically steady state is achieved. The liquid-side flow at Ra = 10^5 does not correspond to fully developed turbulent flow. We then use this solution to initialize the case at Ra = 10^6, where the convective rolls break down into a more chaotic flow. This procedure significantly reduces the time required for a simulation to become statistically steady - when compared, for example - to initializing a quiescent fluid with a linear temperature profile.

We run simulations for 50 free-fall time units, and then take statistics over 50 more. This is less than that often quoted in the literature [**Foroozani**]. However, we only begin taking statistics once the interface temperature is stabilized.

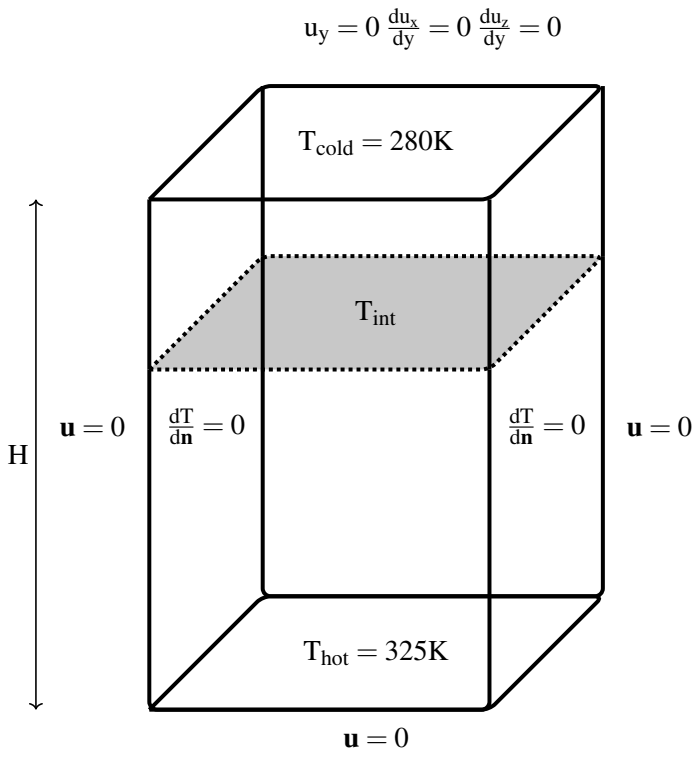

Figure 2 **Computational domain for the VOF simulation** : Velocity boundary conditions are no-slip at all walls except the upper boundary which is set to free slip. The interface divide is such that the liquid-side domain is cubic. The simulation is initialized with a solution at a lower Ra to reduce the time until a statistically steady solution is found

Results

To analyze the system response we again assess the Nusselt numbers in the liquid and gaseous domains. However, as we have two distinct convective flows, we define phase dependent Rayleigh and Prandtl numbers. The definition of Nu_y is the same as equation (19) but the reference value for non-dimensionalization are also phase dependent. This is summarized in Table 2.

The Nu_y values shown in Table 2 are averages of the boundary layers. Equation (20), a phase-dependent volume-averaged Nusselt number, is also provided.

$$Nu_{vol} = \sqrt{RaPr}\,\langle\hat{\rho}\hat{v}\hat{T}\rangle_{xyzt} - \frac{\partial\langle\hat{T}\rangle_{xzyt}}{\partial\hat{y}}\,. \tag{20}$$

Gas-side dynamics

Figures 3 and 4 show a single convective roll in the gaseous phase established early on in the simulations. There is no turbulent wind formation due to the small Ra of 10^4, which is not yet

Phase	Ra	Pr	ρ_{ref}	u_{ref}	y_{ref}	Nu_y	Nu_{vol}
Gas	10^4	0.7	1.1	0.14	$\frac{H}{3}$	2.5	2.6
Liquid	10^6	3.4	988	0.011	$\frac{2H}{3}$	9.9	10.9

Table 2 **Reference values for non-dimensionalization parameters** : Simulation and non-dimensionalization parameters for the two-phase case. The Nu_y provided here is a mean value from 10 samples in the upper and lower boundary layers

turbulent. This is the case despite the significant ΔT that exists between T_{cold} and T_{int}. For RBC the transition to turbulence, and hence plumes and LSC formation, occurs at $Ra \approx 10^5$.

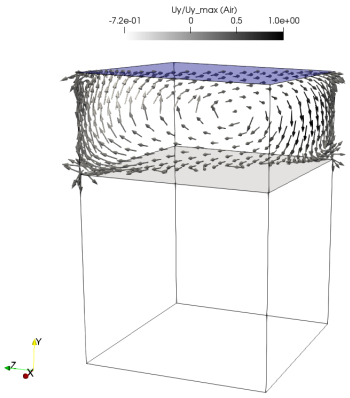

Figure 3 **Gas-side convective roll in diagonal plane 1**

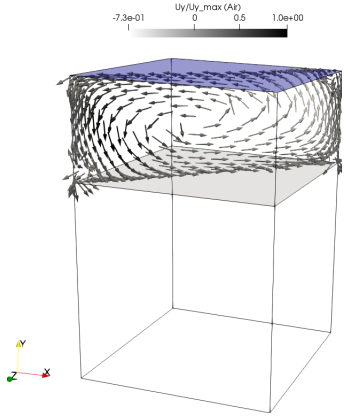

Figure 4 **Gas-side convective roll in diagonal plane 2**

Accordng to energy-balance considerations, when the flow becomes statistically stationary, the vertical profile of the Nu is constant; see also [**Kimmel**]. From Table 2 we see that the gas-side solution is essentially steady; the area-averaged Nu_y and volume-averaged Nu_{vol} values are almost constant. Further, the converged value matches well with the results from the literature for classical RBC (relations from [**Foroozani**], [**Peng**] and [**Niemela**] predict $2.2 < Nu < 2.7$).

It appears that the gas-side flow considered here (low Ra and low Pr) is only mildly influenced by the lower boundary condition. This is due to the significant difference in density between gas and liquid and the stationarity of the interface. The lighter phase perceives the stationary interface as a pseudo-solid surface and thus neither the hydrodynamic nor the thermal boundary layers are impacted by the replacement of the rigid wall by the interface. We note that the stationarity of the interface is unlikely to represent that of an SFP where upward currents from fuel assemblies below would interact directly with the free surface and potentially introduce flow patterns gas-side which are not represented in Figures 3 and 4.

Liquid-side dynamics

There is some variation in Nu_y along the vertical direction possibly due to the fact that the flow has not quite become stationary in the liquid side. This a result of the heat transfer near the boundary plates approaching steady-state quicker than the heat transfer in the bulk; see also [**Kimmel**].

The time-averaged velocity vector field in Figure 5 shows the LSC formation with the two zones of recirculation in the upper and lower corners. This is the typical LSC formation seen in RBC in cubic containers.

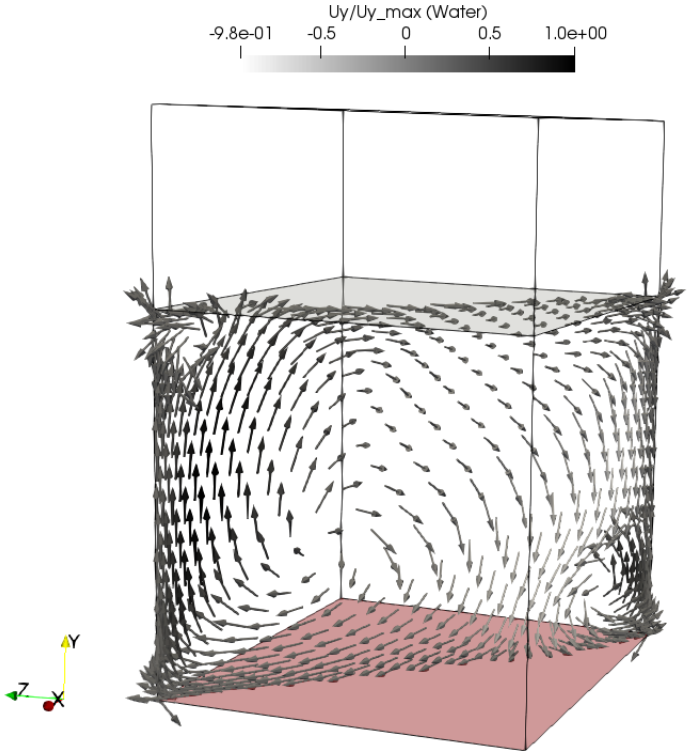

Figure 5 **Liquid-side LSC in diagonal plane** : The typical single LSC that takes the shape of the "container" and the two zones of recirculation in opposite corners are observed.

The liquid-side Nu_y value of 9.9 is higher than that seen in the rigid wall case. This is expected due to the fewer number of hydrodynamic boundary layers in the domain. Indeed, a well converged DNS of the same set-up as in Section 5 but with the upper boundary updated to free-slip produces a (steady and constant) Nu_y of 10.4 and a similar LSC (see Figure 6).

We note that T_{int} continues to rise during the simulation and consequently the Rayleigh number continues to fall. The interface temperature reaches a value within 1K of the temperature at the bottom wall, which is however still sufficient to maintain the liquid-side at $Ra = 10^6$. This suggests that when free-surface evaporation is also considered, the latent heat removal and hence subsequent

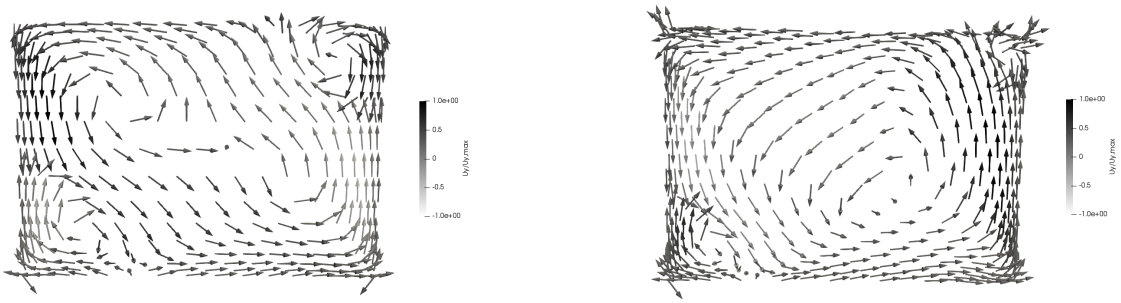

Figure 6 **LSC formation** : Ra^6 with free-slip upper boundary (left) and Ra^6 with free surface (right)

reduction in interface temperature will have an important role on the liquid-side turbulent flow field below.

One further observation is that the interface does not appear to wrinkle during the simulation at $Ra = 10^6$, suggesting that liquid-side turbulence effects are unlikely to impact the free-surface area and hence unlikely to have a significant impact on evaporation rates. This is a point that we plan to investigate in more detail in future studies. During all our two-phase simulations, small vortices formed where the interface meets the corners of the adiabatic side-walls. We argue that they do not have a significant influence on the liquid-side solution, but subsequent studies are required to further investigate their nature and significance.

Finally, it is noted that the geometric simplification of simulating the fuel racks as a uniformly heated flat bottom wall significantly simplifies the SFP physics. The upward flow currents that would be emanating from fuel asemblies below are not captured and this would likely cause significant surface deformations not captured in our simulations.

Conclusions

A low-Mach number VOF solver has been developed using an updated PISO type velocity-pressure coupling algorithm to account for the non-divergence free velocity field. A validation study was completed for classical RBC with water as the working fluid showing good agreement with the DNS from the literature.

Simulations of turbulent RBC with a free surface were then carried out to investigate the impact of the interface on the two convective flows. The results suggest that the gaseous domain, at least at the low Ra studied here, is not greatly influenced by the interface boundary condition but the liquid-side effects are visible in terms of the heat transfer statistics. Further statistically-steady simulations are required to quantify these effects.

Finally, no significant interface movement was captured in the simulations at $Ra = 10^6$. This suggests that liquid-side buoyancy induced interfacial turbulence is unlikely to create waves capable of increasing free surface evaporation in the RBC set-up with a free surface. However, the modelling

constraint of choosing not to simulate the flow from (or to) fuel assmblies below causes a different predicted behaviour to that which occurs in an SFP-LOCA.

Acknowledgments

The first author thanks Bel V for financially supporting the research. Computational resources have been provided by the supercomputing facilities of the Université catholique de Louvain (CISM/UCL) and the Consortium des Équipements de Calcul Intensif en Fédération Wallonie Bruxelles (CÉCI) funded by the Fond de la Recherche Scientifique de Belgique (F.R.S.-FNRS) under convention 2.5020.11.